Appl. Phys. A (2015) 121:1211–1217
DOI 10.1007/s00339-015-9492-6

Applied Physics A
Materials Science & Processing

The structural behavior of $SrTiO_3$ under 400 keV Ne^{2+} ion irradiation

X. Su[1] · C. G. Liu[1] · D. Y. Yang[1] · J. Wen[1] · E. G. Fu[2] · J. Zhang[3] · L. J. Chen[1] · D. P. Xu[1] · Y. Q. Wang[4] · Y. H. Li[1]

Received: 5 July 2015 / Accepted: 11 September 2015 / Published online: 15 September 2015

Abstract The structural behavior of polycrystalline perovskite $SrTiO_3$ under 400 keV Ne^{2+} ion irradiation at both liquid nitrogen (LN_2) and room temperature (RT) has been investigated. The grazing incident X-ray diffraction technique was applied to examine the radiation-induced structural evolution. The radiation behavior of $SrTiO_3$ depends strongly on the irradiation temperature. At LN_2 temperature, the samples exhibit significant lattice swelling and amorphization, whereas at RT, the lattice swelling is much less conspicuous and no amorphization is detected even at the highest irradiation dose of 5.0 dpa. Nevertheless, Ne^{2+} irradiation induces peak splitting in XRD patterns at both temperatures. Furthermore, first-principle calculations have been performed with VASP, involving possible defect types, to identify which defect is responsible for the radiation effect of $SrTiO_3$. The results reveal that the oxygen vacancy defect is the most likely to contribute to the radiation behavior of $SrTiO_3$.

✉ Y. H. Li
liyuhong@lzu.edu.cn

[1] School of Nuclear Science and Technology, Lanzhou University, Lanzhou 730000, China

[2] State Key Laboratory of Nuclear Physics and Technology, Peking University, Beijing 100871, China

[3] School of Energy Research, Xiamen University, Xiamen 361005, China

[4] Materials Science and Technology Division, Los Alamos National Laboratory, Los Alamos, NM 87545, USA

1 Introduction

Perovskites are the most abundant mineral on earth with the general formula of ABO_3, and strontium titanate ($SrTiO_3$) is a prominent representative of the group. Due to high dielectric constant, good magnetic, ferroelectric and insulating properties, outstanding resistance against oxidation, and chemical and thermal stabilities, $SrTiO_3$ has been of great technological interest in microelectronics and optoelectronic industries and in clean energy research [1–4]. In addition, perovskite oxides, particularly $SrTiO_3$, have been proposed as possible ceramic host phases for immobilization of high-level radioactive nuclear wastes, especially actinide elements and fission-product wastes (such as ^{90}Sr) [5]. During the long-term storage, waste forms are submitted to severe radiations, e.g., the α-decay of actinides and β-decay of fission products. As a result, radiation damage accumulates in the host phases and ultimately reduces the physical and chemical durability [6, 7]. In this regard, it is important to understand and predict the behavior of materials in radiation environment. Generally, high-intensity energetic ion beams are applied to simulate the radiation effects induced by α-events in actual disposal of wastes over a long period of time. Extensive irradiation experiments using various ion species and energies have been completed to investigate the radiation response of $SrTiO_3$, mainly focused on damage accumulation and the critical dose for amorphization [8–12], irradiation-induced epitaxial regrowth due to irradiation with He, Ne, Ar and Si ions [13, 14], surface modification by Ga and Ar ions [15, 16], and recrystallization from Kr, Xe, Au and Pb ions [11, 17, 18]. Sabathier et al. [10] have declared that dose rate and sample temperature are two important factors that can affect $SrTiO_3$ susceptibility to amorphization. Zhang et al. [11] have also quantitatively investigated the damage

evolution as a function of temperature and dose under Au ion irradiation. Moreover, it was found that increased temperature can lead to less irradiation-induced damage due to the high defect recovery rate [19].

However, in this paper, the radiation effect of $SrTiO_3$ under 400 keV Ne ion irradiation at both liquid nitrogen and room temperature has been studied using grazing incident XRD technique, particularly concentrating on the radiation-induced lattice swelling effect and temperature dependence, two critical factors that should be considered when designing the nuclear waste forms in practical applications. Furthermore, in order to investigate the mechanism of structural evolution of the irradiated $SrTiO_3$, first-principle calculations have been performed, taking a variety of possible defects into account.

2 Methodology

Polycrystalline $SrTiO_3$ samples were synthesized using conventional ceramic processing procedures, from TiO_2 (Beijing HWRK Chem Co., LTD, 99.99 % purity) and $SrCO_3$ (Beijing HWRK Chem Co., LTD, 99.99 % purity) as starting materials. The mix powers were ball-milled, pressed into pellets and then sintered at 1100 °C for 24 h. To ensure the reaction proceeds completely and homogeneously, the pellets were re-milled, repressed and re-sintered at 1300 °C for 72 h. The resulted pellets were finally polished to a mirror finish using W0.25 diamond suspension. The synthesized $SrTiO_3$ is proved to be phase-pure, and the measured density is larger than 90 % of the theoretical value (5.106 g/cm^3, obtained from X-ray measurement).

Ion irradiations were performed at the Ion Beam Materials Laboratory, Los Alamos National Laboratory, using a 200-kV Danfysik high-current research ion implanter. The 400 keV Ne^{2+} ion irradiations were performed at normal incidence at ion fluences ranging from 7×10^{14} to 2×10^{16} ions/cm^2 under liquid nitrogen (LN_2) and room temperature (RT), respectively. The average ion flux was $\sim 1 \times 10^{12}$ ions/(cm^2·s). The projected range of the 400 keV Ne^{2+} ions in the cubic $SrTiO_3$ was estimated using the Monte Carlo code SRIM 2008 [20]. The projected range and the longitudinal straggling of Ne in $SrTiO_3$ by SRIM are approximately 456 and 117 nm, respectively, and the maximum displacement damage dose is approximately 0.25 dpa (displacements per atom) at a fluence of 1×10^{15} ions/cm^2 as shown in Fig. 1. In these SRIM calculations, the target density $\rho = 5.106$ g/cm^3 was used and the threshold displacement energies for O, Ti and Sr were chosen to be 45 [21, 22], 70 [23] and 80 [23] eV, respectively.

Grazing incidence X-ray diffraction (GIXRD) was performed in Lanzhou University using a Rigaku D/Max-2400 X-ray diffractometer with Cu-Kα radiation, θ–2θ geometry, and the X-ray incident angle of $\gamma = 1.2°$. The depth of the X-ray in $SrTiO_3$ at $\gamma = 1.2°$ is 0.35 μm which was estimated by using geometrical method [24]. The GIXRD penetration depth almost corresponds to the depth of damaged peak (as shown in Fig. 1). The scan range was 20°–75°, with the step size of 0.02° and a dwell time of one second.

First-principle calculations based on density functional theory were performed to evaluate the formation energy of point defects and the theoretical XRD of the relaxed $SrTiO_3$ structure with different point defects by using the Vienna Ab initio Simulation Package (VASP) with the

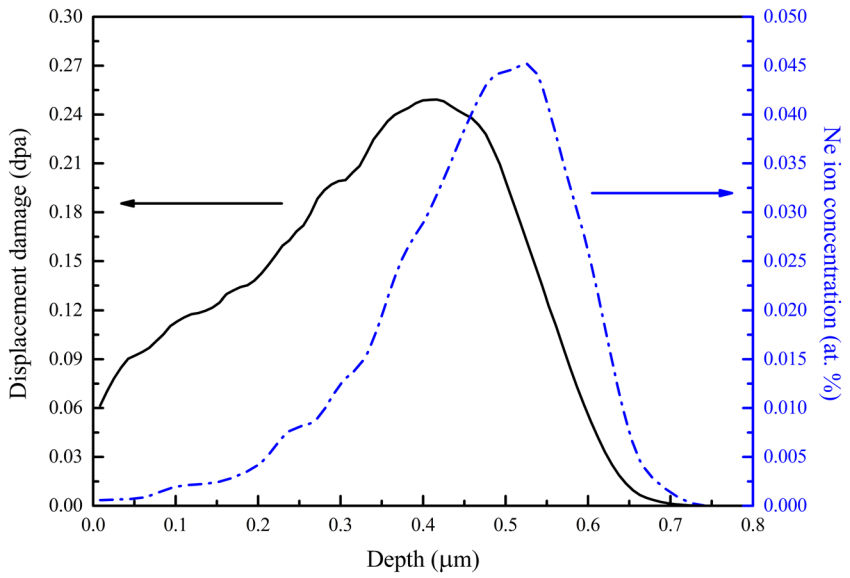

Fig. 1 Damage profile and implanted Ne profile in $SrTiO_3$ with fluence of 1×10^{15} ions/cm^2 under 400 keV Ne irradiation as determined by SRIM calculations

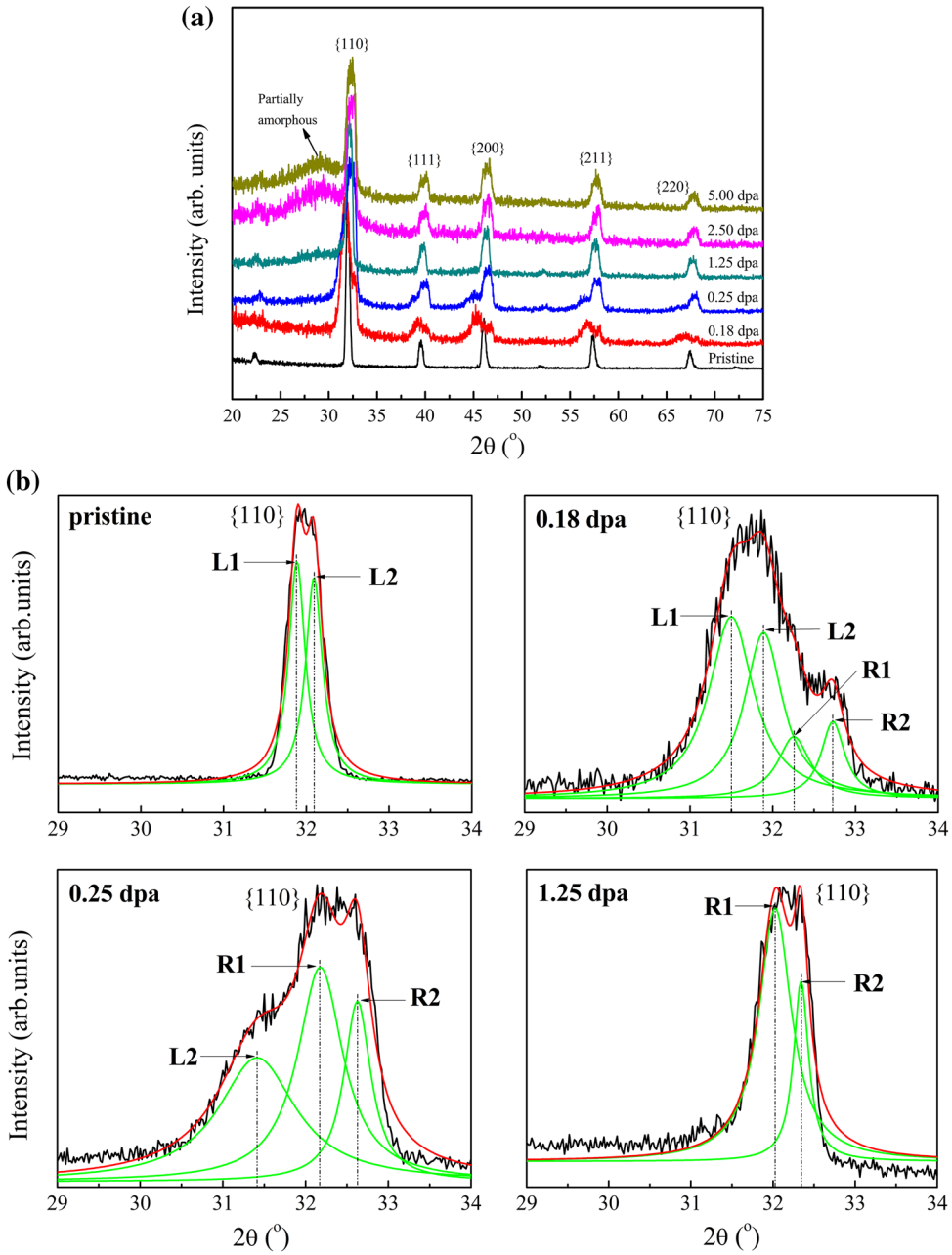

Fig. 2 **a** GIXRD patterns of the pristine and irradiated $SrTiO_3$ under 400 keV Ne^{2+} ions at LN_2 temperature. **b** Data fitting in an enlarged view of the {1 1 0} peak

generalized gradient approximation (GGA) [25, 26]. The interactions were described using the projector augmented wave (PAW) method [27, 28] with PBE functional [29, 30]. The conjugate gradient scheme was used in the relaxing of lattice parameters and internal atomic positions of all structures. The total energies and properties were calculated with 8 × 8 × 8 Monkhurst–Pack *k*-point mesh, and a cutoff energy of 520 eV for the plane wave basis set in the unit cell (five atoms). The calculations for defect formation energies were based on the 4 × 4 × 4 supercell (containing 320 atoms) with 2 × 2 × 2 Monkhurst–Pack *k*-point mesh and a cutoff energy of 520 eV.

3 Results and discussion

Figure 2a shows the GIXRD patterns of the pristine and irradiated $SrTiO_3$ under LN_2 temperature with 400 keV Ne^{2+} ions at fluences of 7×10^{14}, 1×10^{15}, 5×10^{15}, 1×10^{16} and 2×10^{16} ions/cm^2. These ion irradiation fluences were converted into the standard units of dpa, i.e., 0.18, 0.25, 1.25, 2.5 and 5.0 dpa, respectively [31]. For the pristine sample, all the diffraction maxima can be ascribed to the perovskite structure from previous studies [10, 15, 19]. At low-dose irradiation, no significant changes are found from the GIXRD patterns, except for minor shifts of

the diffraction peaks. As the dose reached 2.5 dpa, a broadband (as marked) occurs obviously at the left of {1 1 0} peak. This broadband arises from diffuse scattering of the amorphous phase, which confirms that Ne ion irradiation has induced a crystalline-to-amorphous transformation.

In order to analyze the peak shifts induced by irradiation in detail, each XRD peak of the irradiated $SrTiO_3$ diffraction patterns before amorphization was fitted with Lorenz functions. The fitted XRD patterns are consistent with the previous studies on the cubic $SrTiO_3$ [32, 33]. For an ideal cubic $SrTiO_3$ structure, each diffraction peak consists of two very close side-by-side peaks, as shown in the enlarged view of {1 1 0} peak in Fig. 2b. The {1 1 0} peak of pristine $SrTiO_3$ can be decomposed into two peaks marked by L1 and L2. While for the irradiated samples under 0.18 dpa, new peaks, marked by R1 and R2, emerge at the right of L1 and L2. The presence of R1 and R2 indicates that the structure of $SrTiO_3$ has been changed by irradiation, which may be due to the lattice distortion induced by the formation of defects [31], but it is not sure which type of defect is responsible only from the XRD results. As the irradiation dose increases, the relative intensity of the original peak L1 and L2 decreases gradually. At the dose of 1.25 dpa, the peak L1 and L2 have disappeared in succession, and only R1 and R2 remain, as shown in Fig. 2b. Besides, each peak shifts to smaller 2θ slightly as the irradiation dose increases.

Figure 3a shows the GIXRD patterns of the pristine and irradiated $SrTiO_3$ under RT with Ne^{2+} fluences of 5×10^{15}, 1×10^{16} and 2×10^{16} ions/cm^2, corresponding to 1.25, 2.5 and 5.0 dpa, respectively, and Fig. 3b is the enlarged view of the {1 1 0} peak. Similarly, new peaks (R1 and R2) appear after irradiation under RT, but only L1 disappears at the highest dose of 5.0 dpa. The peaks also shift to lower 2θ under irradiation at RT, which is not as obvious as that at LN_2 temperature. It is worth noting that there is no obvious amorphization observed for the irradiated $SrTiO_3$ under RT even at the highest dose of 5.0 dpa, which is much different from the case under LN_2 temperature.

The shift of the L1 and L2 peak to smaller 2θ is actually indicative of the increase in the lattice parameter [34]. In other words, lattice swelling effect has been induced by Ne^{2+} ion irradiation in $SrTiO_3$. Similar result was gained in the study of Ar ion irradiated $SrTiO_3$ [15]. In order to quantify the lattice swelling as a function of Ne^{2+} ion fluence, the relative variations of lattice parameter $\Delta a/a_0$ (a_0 is the lattice parameter of pristine $SrTiO_3$) were calculated using the similar procedures described in our earlier publications [34], as plotted in Fig. 4. The lattice parameter increases as a function of the irradiation dose in both LN_2 and RT cases. However, the increasing rate at RT is remarkably lower, as compared with the LN_2 case.

According to the above analysis, the radiation response of $SrTiO_3$ induced by 400 keV Ne ions, including amorphization and lattice swelling, depends strongly on the irradiation temperature. The enhanced radiation resistance at RT is probably due to that the dynamic recovery of the irradiation-induced damage increases as the irradiation temperature increases [11, 19]. In fact, the damage process of materials under irradiation is mainly the result of competition between the defect formation and annihilation. At LN_2 temperature, the defects are always inert and possess very low migration rate, and the majority of defects formed can remain. While as the temperature increases, dynamic recovery processes, including defect migration and clustering, become more active. Thus, the chance of defect annihilation is increased significantly. Therefore, the final survival defects are relatively few even though irradiation may produce a large number of defects. The change in the irradiation temperature can dramatically affect the defect accumulation.

In order to elucidate which type of defect is responsible for the radiation effect of $SrTiO_3$, first-principle calculations of the formation energies of possible defect types have been performed systematically. Various point defects have been considered, including the individual vacancies of Sr, Ti and O, the cation antisite defect, and the Frenkel defects of Sr, Ti and O.

The defect formation energy (ΔE_{defect}) is determined as [35]

$$\Delta E_{\text{defect}} = E_{\text{def}} - E_{\text{per}} - \sum_i \Delta n_i \mu_i, \tag{1}$$

where E_{def} is the total energy of a sufficiently large supercell containing the defect, E_{per} is the total energy of a perfect supercell containing the same number of primitive unit cells, Δn_i is the number of atoms of element i added (or removed) to produce the defective structure and μ_i is the chemical potential for the ith element. The chemical potential is defined as the free energy cost of supplying or removing the required number of atoms in an open system [36]. In the case of $SrTiO_3$ system, the chemical potentials are determined from equilibrium conditions of various phases containing Sr, Ti and O. In assumption that $SrTiO_3$ is always stable, the chemical potentials of the three elements can vary in the following correlation:

$$\mu_{\text{Sr}} + \mu_{\text{Ti}} + 3\mu_{\text{O}} = \mu_{\text{SrTiO}_3(\text{bulk})}, \tag{2}$$

where $\mu_{\text{SrTiO}_3(\text{bulk})}$ is a total energy per formula unit of perfect $SrTiO_3$ crystal. If, for example, $SrTiO_3$ is in equilibrium with O and SrO, μ_i is also constrained by the equations as shown below:

$$\mu_{\text{Sr}} + \mu_{\text{O}} = \mu_{\text{SrO(bulk)}}, \quad \mu_{\text{O}} = \mu_{\text{O(bulk)}}. \tag{3}$$

Here, $\mu_{\text{O(bulk)}}$ corresponds to the chemical potential per atom of O_2 gas. Thus, the chemical potentials of Sr, Ti and O can be calculated from the above equations [36].

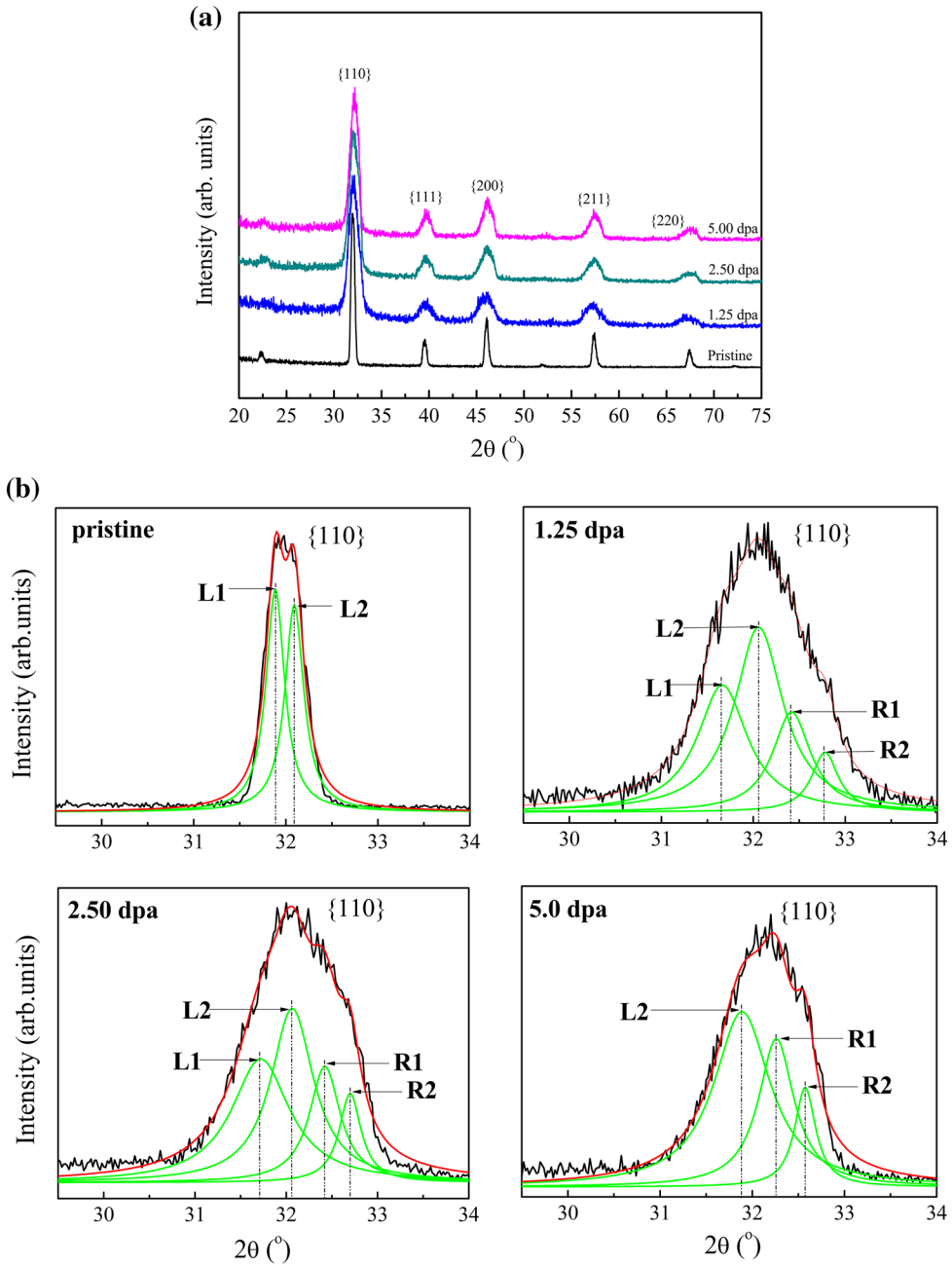

Fig. 3 **a** GIXRD patterns of the pristine and irradiated $SrTiO_3$ under 400 keV Ne^{2+} ions at RT. **b** Data fitting in an enlarged view of the {1 1 0} peak

The calculated defect formation energies are shown in Table 1. It is clear that the formation energy of O vacancy is the smallest among all the defects considered, implying that the formation of O vacancy is the most energetically favorable in $SrTiO_3$ upon irradiation, which is in good agreement with experimental results [15]. Therefore, it can be inferred that the structural evolution of $SrTiO_3$ observed is caused by the O vacancy formation during irradiation. This result is also confirmed by previous studies [37–39] where it is suggested that the oxygen vacancy can be easily introduced into perovskite oxides via various processes. Furthermore, the XRD patterns of relaxed $SrTiO_3$ with different concentrations of O vacancy were simulated, as shown in Fig. 5, which can provide an intuitive approach to compare the results between experiments and first-principle calculations. The simulated XRD patterns of perfect and defective $SrTiO_3$ also show the splitting of diffraction peaks, which is in excellent agreement with the results shown in Figs. 2a and 3a. When the O vacancy concentration reaches to 8/192, new peaks emerge at the right side of the original {1 1 0} peak with most part overlapped. As the content of O vacancy increases to 21/192, the new

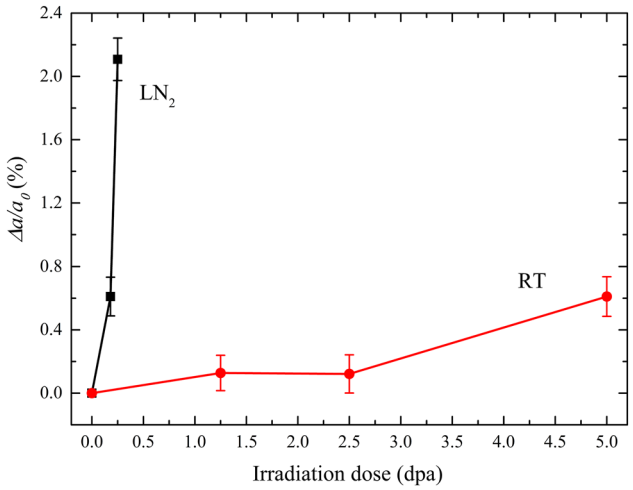

Fig. 4 Relative variation of the lattice parameter, $\Delta a/a_0$, as a function of the irradiation dose under LN_2 and RT

Table 1 Defect formation energies in $SrTiO_3$ calculated using VASP with a 4 × 4 × 4 supercell of 320 atoms

Defect type	Defect formation energy (eV)		
	Oxygen	Strontium	Titanium
Vacancy	4.94	8.16	14.31
Frenkel	4.95	9.52	8.41
Cation antisite		6.27	

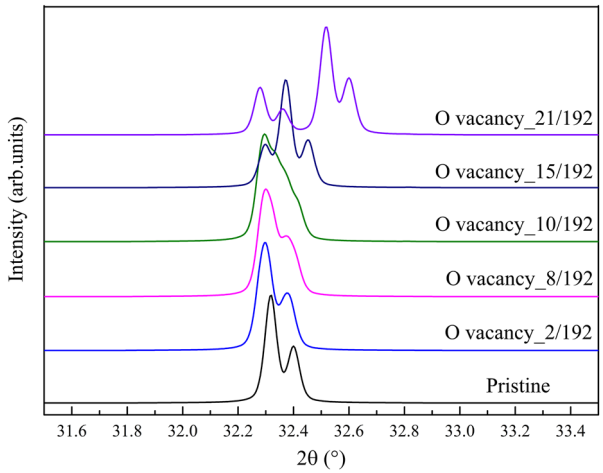

Fig. 5 Simulated XRD patterns of relaxed $SrTiO_3$ structures containing different O vacancies with different concentrations from VASP calculations

peaks can be clearly differentiated from the original ones. More specifically, the simulated XRD suggests that the original diffraction peaks shift to smaller 2θ as the concentration of O vacancy increases. Otherwise, the relative intensity of original peaks decreases obviously with increasing O vacancies. These results agree very well with the observations from GIXRD in our experiments. It should be mentioned that from the simulated XRD patterns, one can see that the position of new emerging peaks to larger 2θ with increasing O vacancy concentration, showing a slight deviation with the experimental results where both R1 and R2 shift to the lower 2θ with increasing irradiation dose. The main reason is probably that, as the irradiation dose increases, more complicated defects would be induced rather than a single species of O vacancy as concerned in our calculation process. However, it is true that under the low-dose irradiation, the splitting and shift of the diffraction peaks are dominantly the result of O vacancy formation. Besides, although we conclude that O vacancy is the primary cause of the structural evolution of $SrTiO_3$ irradiated by Ne^{2+} ions, O anion is a much weaker X-ray scatterer, as compared with Sr and Ti cations. Actually, the introduction of O vacancies can lead to local lattice distortion through the relaxation of Sr and Ti cations, which eventually resulted in different XRD patterns of defective $SrTiO_3$.

4 Conclusions

In summary, polycrystalline perovskite $SrTiO_3$ was irradiated by 400 keV Ne^{2+} ion at both LN_2 and room temperature. Significant structural evolutions have been induced in $SrTiO_3$, including lattice swelling and amorphization. The first-principle calculated results indicate that the O vacancy is the most energetically favorable defect and probably contributes to the structural evolution of irradiated $SrTiO_3$. Moreover, O vacancy can also induce peak splitting and shift of $SrTiO_3$ in the simulated diffraction patterns of the relaxed $SrTiO_3$ structure, which agrees the experimental results very well. Meanwhile, the radiation response of $SrTiO_3$ depends strongly on the irradiation temperature: (1) the lattice parameter of $SrTiO_3$ increases much more rapidly at Ln_2 temperature than that at room temperature; (2) $SrTiO_3$ was severely amorphized at dose of 2.5 dpa under LN_2 temperature, while no amorphization was detected at room temperature even at the highest dose of 5.0 dpa. The enhanced radiation resistance of $SrTiO_3$ to amorphization and lattice swelling at room temperature is mainly due to the enhanced defect annihilation at room temperature. These results are fundamentally meaningful to the application of ceramic nuclear waste forms, since the lattice swelling and temperature effect are closely correlated with the long-term mechanical and thermal durability of waste forms.

Acknowledgments This work was sponsored by the National Natural Science Foundation of China (11475076, 11175076 and 11135002). Ion Beam Materials Laboratory was partially supported by the Center for Integrated Nanotechnologies, a DOE nanoscience user facility jointly operated by Los Alamos and Sandia National Laboratories.

References

1. H. Muta, K. Kurosaki, S. Yamanaka, J. Alloys Compd. **350**(1–2), 292–295 (2003)
2. C.S. Koonce et al., Phys. Rev. **163**(2), 380–390 (1967)
3. J.G. Bednorz, K.A. Müller, Phys. Rev. Lett. **52**(25), 2289–2292 (1984)
4. H.P.R. Frederikse, W.R. Thurber, W.R. Hosler, Phys. Rev. **134**(2A), A442–A445 (1964)
5. W.J. Weber et al., MRS Bull. **34**(01), 46–53 (2009)
6. L.W. Hobbs et al., J. Nucl. Mater. **216**, 291–321 (1994)
7. L. Thomé et al., Adv. Mater. Sci. Eng. **2012**, 13 (2012)
8. A. Meldrum, L. Boatner, R. Ewing, Nucl. Instrum. Methods Phys. Res. Sect. B Beam Interact. Mater. Atoms **141**(1), 347–352 (1998)
9. A. Meldrum et al., J. Nucl. Mater. **300**(2), 242–254 (2002)
10. C. Sabathier, J. Chaumont, J.C. Krupa, Nucl. Instrum. Methods Phys. Res. Sect. B Beam Interact. Mater. Atoms **196**(3–4), 308–314 (2002)
11. Y. Zhang et al., Phys. Rev. B **72**(9), 094112 (2005)
12. Y. Zhang et al., J. Appl. Phys. **100**(11), 113533 (2006)
13. K. Oyoshi, S. Hishita, H. Haneda, J. Appl. Phys. **87**(7), 3450–3456 (2000)
14. S. Nakao et al., Nucl. Instrum. Methods Phys. Res. Sect. B Beam Interact. Mater. Atoms **191**(1–4), 226–229 (2002)
15. K. Daisuke et al., Jpn. J. Appl. Phys. **46**(5L), L471 (2007)
16. J. Albrecht et al., Surf. Sci. **547**(1–2), L847–L852 (2003)
17. C.W. White et al., Mater. Sci. Rep. **4**(2), 41–146 (1989)
18. J. Rankin, B.W. Sheldon, L.A. Boatner, J. Mater. Res. **9**(12), 3113–3120 (1994)
19. M.J. Zhuo et al., J. Nucl. Mater. **442**(1–3), 143–147 (2013)
20. J.F. Ziegler, J.P. Biersack, in *Treatise on Heavy-Ion Science*, vol. 6 (Springer, New York, 1895). pp. 93–129. doi:10.1007/978-1-4615-8103-1_3
21. R. Cooper et al., J. Nucl. Mater. **289**(1), 199–203 (2001)
22. K.L. Smith et al., J. Nucl. Mater. **321**(1), 19–28 (2003)
23. K.L. Smith, N.J. Zaluzec, J. Nucl. Mater. **336**(2), 261–266 (2005)
24. J.A. Valdez, Z. Chi, K.E. Sickafus, J. Nucl. Mater. **381**(3), 259–266 (2008)
25. G. Kresse, J. Furthmüller, Phys. Rev. B **54**(16), 11169 (1996)
26. G. Kresse, J. Furthmüller, Comput. Mater. Sci. **6**(1), 15–50 (1996)
27. P.E. Blöchl, Phys. Rev. B **50**(24), 17953 (1994)
28. G. Kresse, D. Joubert, Phys. Rev. B **59**(3), 1758 (1999)
29. J.P. Perdew et al., Phys. Rev. B **46**(11), 6671–6687 (1992)
30. J.A. White, D.M. Bird, Phys. Rev. B **50**(7), 4954–4957 (1994)
31. Y.H. Li et al., Chin. Phys. Lett. **28**(6), 066102 (2011)
32. J. Hutton, R.J. Nelmes, H.J. Scheel, Acta Crystallogr. Sect. A **37**(6), 916–920 (1981)
33. R.J. Nelmes, G.M. Meyer, J. Hutton, Ferroelectrics **21**(1), 461–462 (1978)
34. Y. Li et al., Phys. Rev. Lett. **108**(19), 195504 (2012)
35. W. Jiang, R.M. Van Ginhoven, D.M. Strachan. *Chemical and Charge Imbalance Induced by Radionuclide Decay: Effects on Waste Form Structure* (Pacific Northwest National Laboratory Richland, WA, 2011). URL: http://www.pnnl.gov/main/publications/external/technical_reports/PNNL-20312.pdf
36. T. Tanaka et al., Phys. Rev. B **68**(20), 205213 (2003)
37. B. Lee et al., Phys. Rev. Lett. **98**(11), 115503 (2007)
38. D. Kan et al., Nat. Mater. **4**(11), 816–819 (2005)
39. K. Potzger et al., J. Magn. Magn. Mater. **323**(11), 1551–1562 (2011)